Temperature and Pressure Dependence of Line Widths and Integrated Absorption Intensities for the O_2 $a^1\Delta_g - X^3\Sigma_g^-$ (0,0) Transition

Stuart M. Newman‡ and Andrew J. Orr-Ewing*

School of Chemistry, University of Bristol, Cantock's Close, Bristol BS8 1TS, U.K.

David A. Newnham and John Ballard

Atmospheric Science Division, Space Science and Technology Department, Rutherford Appleton Laboratory, Chilton, Didcot, Oxfordshire OX11 0QX, U.K.

Received: May 1, 2000; In Final Form: August 14, 2000

The electric-dipole forbidden $a^1\Delta_g - X^3\Sigma_g^-$ (0,0) band of gas-phase O_2 has been studied in absorption at wavelengths around 1.27 μm using Fourier transform spectroscopy and a long-path absorption cell. Experiments were conducted at temperatures of 294, 243, and 200 K and at pressures in the range 140−750 Torr. Both pure O_2 and a mixture of 21% O_2/79% N_2 were studied, and line widths, integrated line intensities, and integrated absorption intensities (AIs) for the (0,0) vibrational band were measured. Integrated AIs were found to be independent of temperature, pressure, and gas composition, and the recommended value for the vibrational band from the current study is $S_{int} = 3.210(15) \times 10^{-24}$ cm molecule^{-1} (1σ error) for pure $^{16}O_2$, corresponding to an Einstein A-coefficient of $A = 2.256(10) \times 10^{-4}$ s^{-1}. The effect of including other oxygen isotopomers is to increase the integrated AI value for this origin band to $S_{int} = 3.226(15) \times 10^{-24}$ cm molecule^{-1}. Widths of individual spectroscopic lines decrease with increasing molecular rotational quantum number. The temperature dependence of Lorentzian line width components, γ_T (fwhm), is well represented by the expression $\gamma_T = \gamma_{294K}(T/294\ \mathrm{K})^{-0.85}$. The effects of pressure broadening of lines by N_2 are indistinguishable from those for pure O_2 at the same temperature and pressure.

1. Introduction

An accurate knowledge of spectral parameters, needed to describe completely molecular absorbances and emissions at reference wavelengths, is of vital importance in atmospheric sensing. Determining the radiative transfer characteristics of a planetary atmosphere requires the locations, intensities, and widths of absorption/emission lines to be well determined, and characteristics such as integrated line intensities may be very sensitive to the wings or overlapping regions of spectral lines.[1] The use of satellite data to probe and quantify atmospheric constituents and properties such as cloud coverage[2] requires detailed information on the dependence of pressure broadening coefficients and line intensities on gas composition, spectroscopic band, and temperature. Even small differences between bands or among colliding molecules may have an important effect on the accuracy of analysis of such satellite measurements.

In the middle atmosphere (the stratosphere and mesosphere), excited $O_2(a^1\Delta_g)$ is not completely quenched by collisions, and one of the strongest features of the day and night airglow emissions is the $a^1\Delta_g - X^3\Sigma_g^-$ (0,0) band at 1.27 μm. During the day, the a−X emission exhibits a peak intensity at altitudes around 50 km, with a typical concentration of $O_2(a^1\Delta_g)$ molecules of approximately 2×10^{10} molecules cm^{-3}.[7] The intensity of the emission drops rapidly after sunset (or during a solar eclipse) indicating a primary photochemical source, attributed to ozone photolysis in the Hartley continuum

$$O_3 + h\nu \rightarrow O_2(a^1\Delta_g) + O(^1D) \quad (1)$$

and the Huggins band for wavelengths up to ∼350 nm:[3,4]

$$O_3 + h\nu \rightarrow O_2(a^1\Delta_g) + O(^3P) \quad (2)$$

Monitoring emission of the $O_2(a^1\Delta_g)$, and also $(b^1\Sigma_g^+)$,[5] products of ozone photolysis thus provides a method for determining middle and upper atmosphere ozone concentrations. While collisional quenching competes with spontaneous emission at lower altitudes, above 85 km the lifetime of O_2 $(a^1\Delta_g)$ molecules is determined almost entirely by the radiative loss.[6] The infrared emission may also be used to probe atmospheric dynamics and meteorology at midaltitudes[7,8] and is crucial to the overall atmospheric heat budget, since the absorption of solar ultraviolet radiation by ozone via (1) is the primary radiative forcing mechanism in the mesosphere.[8]

Atmospheric absorption of 94% of the 1.27 μm band airglow emission intensity often (with some exceptions[9]) limits ground based observations to the study of the weaker, but less attenuated, (0,1) band at 1.58 μm.[6,10] Observers must usually rely on aircraft, balloon, rocket-borne[11,12] or satellite instruments to measure the (0,0) band emission; for example, the near-infrared spectrometer on the Solar Mesosphere Explorer (SME) satellite made measurements between 50 and 90 km.[13] As well as being employed for studies of the terrestrial atmosphere, the 1.27 μm dayglow has been used to investigate ozone abundances on Mars[14] and Venus.[15]

* Author for correspondence. Tel: +44 117 928 7672. Fax: +44 117 925 1295. E-mail: a.orr-ewing@bris.ac.uk.

‡ Current address: Meteorological Research Flight, The Met. Office, Y46 Building, DERA, Farnborough, Hampshire GU14 0LX, U.K.

10.1021/jp001640r CCC: $19.00
Published on Web 09/29/2000

In addition to processes (1) and (2), collisional cascade from the O_2 ($b^1\Sigma_g^+$) state is a source of O_2 ($a^1\Delta_g$).[7,16] The probability for optical excitation of O_2 on the $b^1\Sigma_g^+ - X^3\Sigma_g^-$ transition is larger than for a−X absorption by a factor of ∼400, so the $b^1\Sigma_g^+$ state is readily populated by absorption of sunlight at 762 nm (the O_2 b−X (0,0) band center wavelength). Detailed studies of the interconnected processes involved in the creation and destruction of oxygen species in the middle atmosphere have been performed by Mlynczak and co-workers.[8,17] If the 1.27 μm volume emission rate is to be used as a proxy for ozone, it is essential that all the kinetic and spectroscopic parameters affecting $O_2(a^1\Delta_g)$ emission are accurately known. A photochemical model[17] with 26 parameters is needed to describe the infrared airglow completely; the parameters include rates for photolysis, absorption, collisional quenching, and spontaneous emission of various states of $O_3/O_2/O$. Ozone levels may be inferred from the airglow to within 15% at altitudes below 92 km, however, if just six key parameters (including the Einstein A-coefficient for O_2 a−X spontaneous emission) are known to within 7% accuracy.

A precise evaluation of the parameters describing the O_2 $a^1\Delta_g - X^3\Sigma_g^-$ (0,0) spectral band is vital for atmospheric model calculations of radiative transfer, heat budget, and ozone abundances inferred from the O_2 a−X 1.27 μm emission. Laboratory studies have largely focused on room-temperature measurements with high (∼1 atm) concentrations of pure O_2, but such conditions do not coincide with the actual pressure, temperature, and gas-composition conditions encountered in the middle atmosphere: for instance, at an altitude of 30 km, pressure $p \approx 10$ Torr, and temperature $T \approx 225$ K.[18,19] With major terrestrial atmospheric constituents of N_2 (78%) and O_2 (21%),[20] possible effects of oxygen−nitrogen interactions on the atmospheric O_2 a−X spectrum should be examined, but a careful survey of the literature suggests that previous studies of the O_2 $a^1\Delta_g - X^3\Sigma_g^-$ transition have dealt solely with pure O_2.

There have been long-standing uncertainties in the radiative decay rate (described by the Einstein A-coefficient) for $O_2(a^1\Delta_g)$.[21−28] The Einstein A-coefficient is derived from integrated absorption intensity (AI) values (also commonly referred to as integrated band strengths, S_{int}). A detailed summary of studies prior to 1998[29] cites a value of $A = 2.59 \times 10^{-4}$ s^{-1} (corresponding to a radiative lifetime of 64.4 min) based on unpublished results from Brault and Brown.[30] This value agreed with the early study of Badger et al.[21] and was included in the 1996 HITRAN database.[31] Mesospheric observations also lend support to this value.[32] Three recent studies have, however, established a consensus for a different A-coefficient: Lafferty et al.,[33] used Fourier transform spectroscopy (FTS) coupled to an 84 m multipass cell to obtain $A = 2.237(51) \times 10^{-4}$ s^{-1} (and hence a lifetime of 74.4 ± 1.6 min). We have measured integrated band strengths and Einstein A coefficients by both FTS and cavity ring-down spectroscopy (CRDS)[34] and obtained $A = 2.19(5) \times 10^{-4}$ s^{-1} and $2.14(7) \times 10^{-4}$ s^{-1}, via the two independent techniques. Most recently, Cheah et al.[29] reported an integrated AI from FTS experiments that converts to $A = 2.28(5) \times 10^{-4}$ s^{-1}. These measurements, although performed at a range of O_2 pressures, have been restricted to ambient temperatures and to pure O_2 samples.

The present study extends the understanding of the O_2 a−X system by analysis of spectra recorded with both pure O_2 and O_2/N_2 air samples, over a range of temperatures and pressures. The new data reveal p, T, and gas-composition trends in rotational line widths, line-center frequency shifts, and intensities in the O_2 $a^1\Delta_g - X^3\Sigma_g^-$ (0,0) band which are of significance for the correct interpretation of atmospheric airglow observations.

2. Experimental Section

O_2 a−X absorption spectra were recorded for static gas samples using the long path absorption cell (LPAC) and Fourier transform spectrometer (Bruker IFS 120 HR) at the Rutherford Appleton Laboratory (RAL), and these instruments have been described in detail elsewhere.[34,36] The broadband white light source used in the spectrometer is a 150 W quartz tungsten halogen lamp (Osram HLX64610). The interferometer of the FT spectrometer has a maximum optical path difference (MOPD) of 600 cm, corresponding to an ultimate resolution of 0.0015 cm^{-1}. The LPAC is a gas absorption cell equipped with White multipass optics and consists of two concentric stainless steel shells, with vacuum between to isolate thermally the inner cylinder containing the gas sample. Radiation exiting the cell is directed through a narrow band-pass optical filter (center wavelength 1.27 μm, fwhm ≈ 39 nm) and is then tightly focused onto the element of a liquid nitrogen cooled indium antimonide detector. A dedicated computer controls the data acquistion, co-adds the interferograms, and applies a fast Fourier transform (FFT) with boxcar interferogram truncation to produce a spectrum.

A cryogenic system allows the inner vessel of the LPAC to be cooled to any temperature between 190 and 300 K, and the cell can be stabilized at a given temperature for an extended period of time. Its central feature is a heat exchanger, which uses liquid nitrogen to cool a circulating fluid (halon 2402, dibromotetrafluoroethane, freezing point 163 K) in an enclosed system. A programmable microprocessor controls a valve to regulate automatically the liquid nitrogen flow rate. The LPAC mirrors are disengaged from thermal contact with the outside environment to minimize temperature-induced drift and hence signal degradation. The temperature inside the LPAC may be regularly monitored by automatic logging of readings from strategically placed platinum resistance thermometers, accurate to ±0.2 K. A calibrated 1000 Torr (±0.08% accuracy) full-scale capacitance manometer (MKS type 390) is used to record the LPAC gas pressure.

The experimental technique used to obtain the ambient temperature (294 K) spectra was very similar to that presented in our previous study.[34] For the reduced-temperature measurements (at ∼243 and 200 K) a slightly lower spectrometer resolution was chosen to increase the speed efficiency of the data acquisition. The extended time periods required to reduce and stabilize the LPAC gas temperature necessitated shorter scan durations for this set of experimental conditions. Thus, an instrument resolution (0.9/MOPD) of 0.010 cm^{-1} was chosen for lower temperature measurements, compared with 0.0058 cm^{-1} at 294 K; this was found not to degrade significantly the quality of the recorded spectra and still enabled individual rotational lines to be adequately resolved for a full analysis. As well as certified purity (99.999%) pure oxygen, a gas mixture of 79% N_2 and 21% O_2, with the generic name "zero" grade synthetic air (Air Products), was also studied. Table 1shows the p, T, and gas-composition conditions at which spectra were recorded.

3. Analysis

3.1. Baseline Corrections to Spectra. The raw spectroscopic data obtained under all the conditions listed in Table 1 were converted to transmittance spectra by removal of the effects of the band-pass filter transmission curve. This background

TABLE 1: Summary of Experimental Conditions Applicable to the Work Presented in the Current Study[a]

instrument resolution/cm^{-1}	gas composition	temp/K	pressure/Torr
0.0058 cm^{-1}	100% O_2	294.0(6)	750.1(5)
		294.0(11)	375.0(5)
		294.0(11)	149.9(5)
	21% O_2/79% N_2	293.8(11)	750.0(3)
		293.8(12)	375.1(5)
		293.7(4)	150.0(5)
0.010 cm^{-1}	100% O_2	243.2(5)	750.7(4)
		241.7(8)	154.4(6)
	21% O_2/79% N_2	243.0(6)	750.2(5)
		244.0(16)	149.8(14)
	100% O_2	198.7(8)	375.7(5)
		200.5(8)	150.4(3)
	21% O_2/79% N_2	201.8(21)	747.7(32)
		199.1(11)	143.6(8)

[a] Typically 500−600 scans were co-added to produce spectra with sufficient signal-to-noise ratios. The 1σ standard errors of the final significant digit(s), in parentheses, are determined from the experimentally measured variations in pressure and temperature and the known instrumental uncertainties.

elimination can, in principle, be achieved either by dividing by a background spectrum (measured under identical conditions except with the LPAC evacuated) or by a polynomial function which simulates the nonabsorbing background. The latter method was preferred in this study because of difficulties of reproduction of the transmission spectrum of the filter at different pressures. The resultant spectra showed sinusoidal baseline oscillations upon which the weak spectral features of interest were superimposed. The baseline oscillations, or "channel spectra" resulted from multiple reflections of the spectrometer light beam between the surfaces of plane-parallel optics (optical filter and windows) in the path between source and detector. Attempts to minimize the baseline modulation by changing the position or tilt of the optical filter were largely unsuccessful. After removal of the gross background baseline, it is important to be able to eliminate channel spectra in order to measure line shapes and absorption intensities quantitatively. In some cases it was possible to model the oscillations by a simple superposition of two or three sine waves with different amplitudes and frequencies; sometimes the oscillatory pattern was more complex, however, and a more sophisticated method was required to model the wave pattern. The frequencies of the oscillations were clearly evident as spikes in the original interferograms. Numerical correction by removal of the peaks in the interferogram, although a recognized method,[37] was not used because of concerns that extensive editing of the interferogram might remove spectral information and introduce unwanted artifacts (such as distorted line shapes) into the spectral domain. Instead, the interferograms were analyzed to deduce the individual oscillation frequencies, and then sine waves of the appropriate frequencies and phases were amplitude fitted to the spectral baselines (in regions of negligible absorption) using the least-squares method. The fitted waveforms were then subtracted from the spectra. This procedure is illustrated in Figure 1 and, though very similar in effect to editing the interferogram, did not appear to introduce spurious spectral anomalies or distort spectral line shapes, but did successfully eliminate the oscillatory baseline. Any effects of the underlying O_4 continuum absorption were subtracted prior to determination of O_2 monomer band intensities, so will not contribute to the values listed in later sections and tables. Spectra were converted

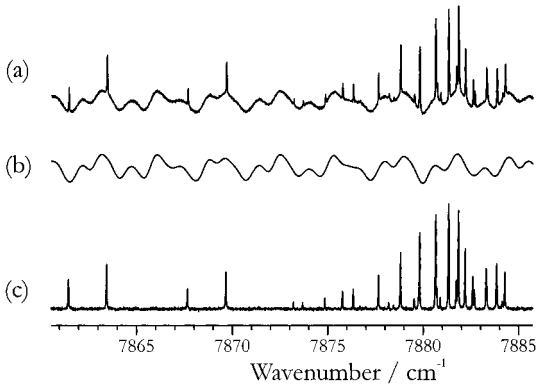

Figure 1. (a) A portion of the FT spectrum of 152 Torr of zero air, corrected for the band-pass filter profile and O_2-O_2 collision induced absorption, but with severe oscillatory structure affecting the spectrum. (b) Underlying oscillations modeled by analysis of the interferogram, as described in the text. (c) Final spectrum, with the background oscillations shown in part (b) subtracted from the spectrum in part (a).

from transmittance, $T(\bar{\nu})$, at a wavenumber $\bar{\nu}$ to Napierian absorbance using $A_e(\bar{\nu}) = -\ln T(\bar{\nu})$.

3.2. Rotational Line Shapes. There are three main constituents contributing to the overall shape of a single, unblended rotational line of O_2 in the a−X band recorded by the FT spectrometer:

(i) A Gaussian line shape component, due to Doppler broadening, with a fwhm that varies with temperature. The calculated fwhms for $^{16}O_2$ at band center (7883 cm^{-1}) at the different experimental temperatures are 0.01712 cm^{-1} at 294 K, 0.01556 cm^{-1} at 243 K and 0.01412 cm^{-1} at 200 K. During line shape analysis, Doppler widths were corrected for the slight changes with transition wavenumber.

(ii) A Lorentzian contribution due to collisional broadening, varying with gas number density from less than 0.02 cm^{-1} fwhm to greater than 0.15 cm^{-1} over the range of p, T conditions used here.

(iii) An instrumental line shape function which, for an ideal FT spectrometer with no additional numerical apodization, is characterized by a sinc function dependent on the spectrometer optical path difference. Scans were performed at two optical path differences, resulting in high resolution (0.0058 cm^{-1}) and, for the lower temperature experiments, lower resolution (0.010 cm^{-1}) spectra.

Each unblended rotational line shape will be a convolution of the inherent natural line shape (of negligible width) with the above functional forms. To quantify the effect of the instrumental line shape on measured spectral lines, convolutions of the instrumental sinc function with Lorentzian lines of varying widths were fitted to unperturbed Lorentzian line shapes. It was found that the convolved line shape ceased to be well represented by a pure Lorentzian function only when the width of the central lobe of the sinc function became comparable to the width of the Lorentzian function. Even at the lowest pressures investigated, the contribution of the instrumental line shape to the spectral line profiles and widths was established to be negligible, and thus rotational lines were fitted only to convolutions of Gaussian and Lorentzian components (i.e., Voigt profiles).

The PGOPHER program[38] was used to simulate individual rotational lines from the various O_2 $a^1\Delta_g - X^3\Sigma_g^-$ (0,0) band spectra and then to perform least-squares fits of the experimental lines (represented as Napierian absorbance) to Voigt profiles. The required input parameters were an estimated line-center wavenumber value, the known Gaussian Doppler width for a given wavenumber and temperature, and a first-guess Lorentzian

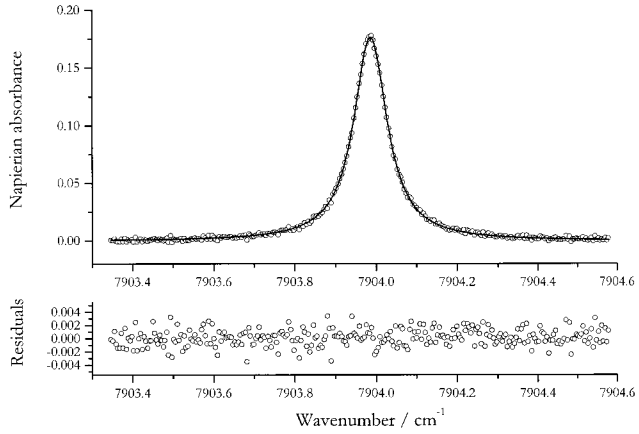

Figure 2. Sample Voigt profile fit to a rotational line, $^{R}R(N'' = 7)$ (notation $^{\Delta N}\Delta J(N'')$) recorded with 750 Torr of O_2 at 294 K, presented with the (observed − calculated) residuals. The absence of systematic deviations in the residuals plot suggests that the line shape is adequately represented by the Voigt function.

width. The floated parameters were the wavenumber offset (the discrepancy between the input line-center wavenumber and the more accurate fitted value), the fwhm of the Lorentzian linebroadening function, the vertical scaling (which establishes the normalized line intensity), and a vertical offset. These parameters were floated simultaneously in the fits and an example of a least-squares fit to a rotational line shape is shown in Figure 2; the line shape is seen to be modeled well by a Voigt profile, with apparently random residual errors. More sophisticated line shape functions such as Galatry and Rautian profiles have been used[39] for rotational line analysis and consideration of these forms is important when the spectral signal-to-noise is sufficiently high to warrant it.[40] However, in the current study the Voigt profile accounts for the observed line shapes very satisfactorily.

3.3. Integrated Band Absorption Intensities. Absorption lines in the baseline-corrected spectra, converted to Napierian absorbance, were integrated over the wavenumber range of interest. Integration was performed in two ways, (i) by fitting Voigt profiles to unblended lines and (ii) by summing numerically the intensity across lines, as described in our previous study.[34] In the latter case, care needs to be taken to ensure that regions which are fitted as baselines are truly representative of zero absorbance. Neglect of the tails of Lorentzian-dominated line shapes can lead to serious systematic errors: for a Lorentzian function with fwhm 0.10 cm^{-1}, 0.6% of the spectral intensity lies more than 5 cm^{-1} away from the line-center wavenumber, and 1.6% lies more than 2 cm^{-1} away. Often the spectral lines are spaced more closely than this. The solution to baseline measurement adopted here was to fit a few widely spaced spectral regions to determine the baseline to be subtracted to establish a zero of absorbance. This method introduces unavoidable (random) errors in baseline levels, especially in the band-head regions where the majority of the spectral intensity lies, but was nevertheless judged to be the method least likely to introduce systematic inaccuracies in the final integrated AI values derived by method (ii).

There are further additional possible sources of significant error in the numerical integration analysis method. Neglect of very weak lines which are indistinguishable from the baseline noise may lead to systematically low values for integrated band intensities. However, with the relatively high signal-to-noise ratios obtained in this work, this is expected to introduce an error of less than 0.4% in all cases (based on theoretical line intensities). For scans carried out under conditions of low pressure and/or zero air, the maximum signal is reduced, with a necessarily higher random error in the integration. These errors have been estimated from the reproducibility of the integrated band strengths and propagated into the final error estimates. Finally, regardless of data analysis method, linear detector response is essential for accurate data acquisition because for the most favorable signal-to-noise conditions, peak signal represents a reduction of as much as half in transmission of light through the spectrometer. The use of small apertures in the FT spectrometer, together with the light losses in the LPAC and transfer optics, reduced the light intensity to levels far below those at which InSb detector or preamplifier saturation and nonlinearity occurs.

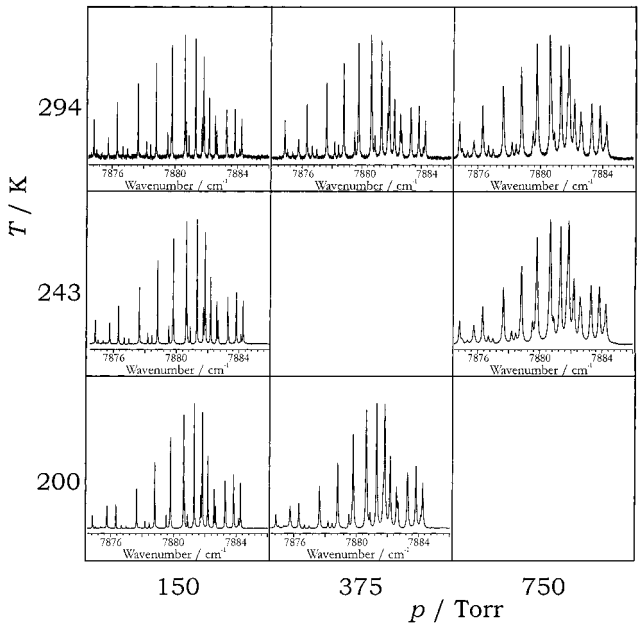

Figure 3. Pure O_2 $a^1\Delta_g - X^3\Sigma_g^-$ (0,0) band spectra (band head region only) illustrating the changes in rotational line width and intensity distribution as a function of temperature and pressure. No pure O_2 spectra were recorded for 243 K/375 Torr and 200 K/750 Torr. The 294 K spectra appear noisier due to the higher resolution of these scans.

The method of individual line-fitting to obtain integrated AIs is discussed further in section 4.3. A comparison is made in section 5.2 between the accuracies, advantages, and disadvantages of the two integration methods.

4. Results

All experimentally recorded spectral lines sufficiently strong to allow a quantitative analysis were fitted to Voigt line shape functions, providing values for line widths, center wavenumbers, and integrated intensities. In practice, due to changes in the Boltzmann distribution of energy level populations with temperature, this allowed lines up to around $N'' = 25$ to be analyzed at 294 K, and up to $N'' = 21$ and $N'' = 17$ at 243 and 200 K, respectively. The Voigt profile fitting routine did not allow simultaneous fitting of multiple lines with varying widths, so blended, overlapping line shapes were either not fitted at all, or else fits were performed on partial line shapes that could be attributed reliably to a single spectral line.

Samples of spectra recorded at various temperatures and pressures of pure O_2 are shown in Figure 3. Line broadening with increased pressure and more intense higher-N rotational progressions at higher temperatures are both visible. More quantifiable dependencies are revealed by individual line fits. The large amount of data generated,[41] which encompasses line center wavenumbers, line widths, and integrated line and band

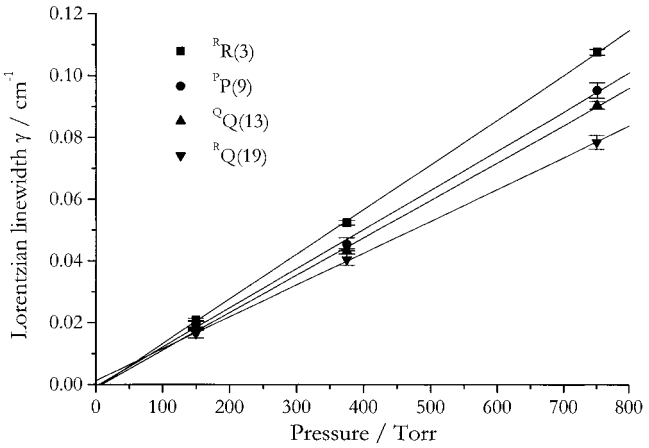

Figure 4. Plot of fwhm Lorentzian line width versus O_2 sample pressure for four rotational lines identified by the notation $^{\Delta N}\Delta J(N'')$ at three separate pressures at 294 K. The values for each transition have been fitted to a straight line and extrapolated back to $p = 0$, giving $\gamma_0 = 0$ to within the experimental error.

AIs at all *p*, *T*, and gas compositions studied, is available upon request from the authors. The following sections emphasize the most important details of our results.

For all measurements, pressures and temperatures were regularly monitored. Small drifts in both these quantities were observed (and were exacerbated at lower temperatures by the difficulties in stabilizing the conditions). A straightforward estimation of uncertainties was given by the standard deviation about the mean of the spread of values of experimental parameters. For temperature measurements there is an additional uncertainty of ± 0.2 K from the instrumentation, and a further error of $\pm 0.08\%$ for pressures. The propagation of errors into variables dependent on the observables was quantified using standard expressions.[42] The calculation of S_{int} depends on path length *L*, but this quantity is determined to much higher precision[43] (128.75 ± 0.18 m) than other variables, and this error was neglected in overall error estimates. The final standard deviation errors determined for S_{int} values include estimates for the errors associated with the numerical integration process, based on reproducibility, and these errors were propagated in the same fashion.

4.1. Line Widths. The Lorentzian fwhm for individual spectral lines are listed in an appendix of ref 41 and are available from the authors for all the experimental conditions listed in Table 1. The results presented here are primarily in graphical form for reasons of space. For the 294 K measurements three different pressures of each gas (O_2 and zero air) were investigated; two separate pressures were studied for the subambient temperatures.

It is expected that the measured Lorentzian line width components at any given temperature should be proportional to the gas pressure. Under such circumstances the gradient of a straight line plot of Lorentzian line width versus pressure *p* gives the pressure broadening coefficient for a given rotational line. To assess the validity of this relationship, the fwhm line widths (γ) for four distinct rotational lines (from pure O_2 spectra at 294 K) are plotted against pressure in Figure 4. These lines are characterized by varying degrees of signal-to-noise and span a wide range of rotational quantum numbers. A straight line has been fitted through the data points for each transition, and in all cases intercepts the graph origin to within experimental error. Thus, the relationship $\gamma \propto p$ is obeyed at 294 K and, by inference, at 243 and 200 K.

Pressure broadening coefficients may be derived for all lines by measuring the gradient of plots such as those shown in Figure 4. In practice, given that the assumption of a linear trend in Lorentzian line width with pressure, coinciding with the graph origin, is valid, the data sets for separate pressures, but otherwise identical experimental conditions, may be combined by scaling them all to unit (1 atm) pressure and calculating an average for each rotational line. If η is the pressure broadening coefficient (i.e., $\gamma_p = \eta p$) then finding the scaled line width at 1 atm, $\gamma_{1atm} = \gamma_p/p$, is equivalent to determining η. Weighted averages of γ_{1atm} values obtained from data at different pressures for each rotational line may then be calculated to obtain more accurate values of γ_{1atm} (or η).

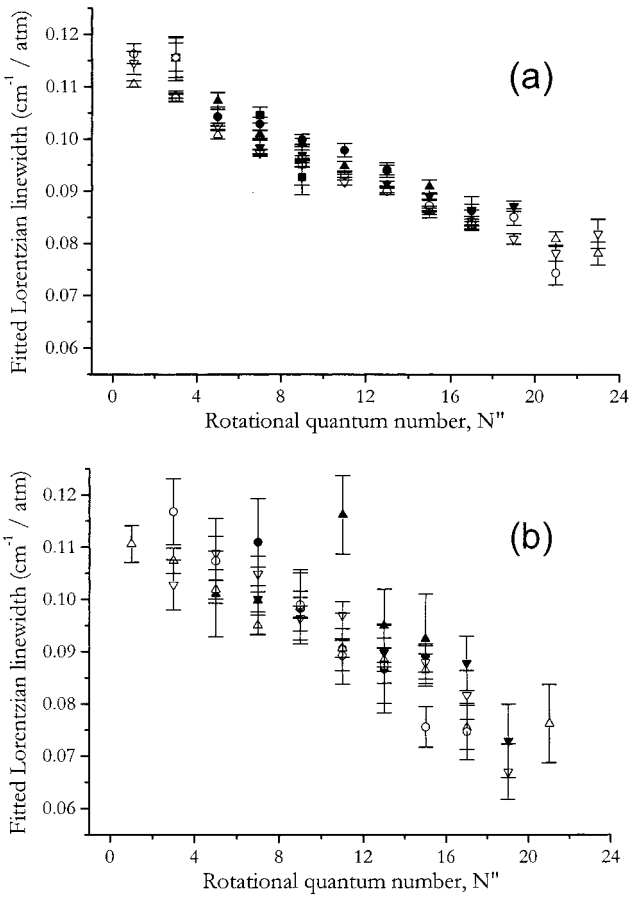

Figure 5. Graphs displaying fitted line widths for (a) pure O_2 and (b) zero air at 294 K. Measurements at different gas pressures have been combined to produce the data points and error bars as described in the text, with all values scaled to 1 atm. Data points with relative errors greater than 5% in (a) and 10% in (b) have been excluded for the purposes of clarity. Line widths for lines from the various spectroscopic branches are represented by the following symbols: ■ ^{O}P; ● ^{P}P; ▲ ^{P}Q; ♦ ^{Q}P; ▼ ^{Q}Q; ◊ ^{Q}R; △ ^{R}R; ▽ ^{R}Q; ○ ^{S}R.

Figures 5−7 show the results of the above manipulations, with measured spectral line widths, scaled to a pressure of 1 atm, plotted against rotational quantum number (N'') for the six different combinations of temperature and gas composition used in the current study. Data are plotted for a total of 9 distinct spectroscopic branches. Some (weaker) lines have large errors, so a cutoff criterion is needed to clarify the details of the graphs. A 10% relative error ($\sigma_{ave}/\gamma_{ave}$) is the maximum included; for the highest signal-to-noise measurements most data points had errors of 5% or less, so this is the upper bound for inclusion in those cases.

The figures show that for both the O_2 and zero air data sets there are strong trends in derived Lorentzian line widths, which decrease monotonically with rotational quantum number. There is also a lesser line width dependence as a function of rotational

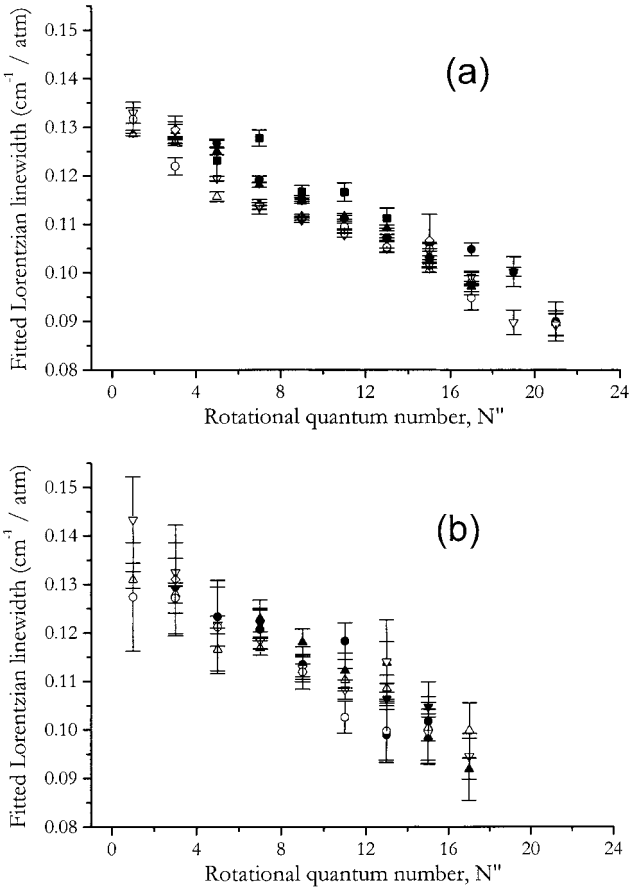

Figure 6. Graphs displaying fitted line widths for (a) pure O_2 and (b) zero air at 243 K. All values have been scaled to 1 atm unit pressure. Data points with relative errors greater than 5% in (a) and 10% in (b) have been excluded from the graphs. Symbols used to denote spectroscopic branches are the same as in Figure 5. Note the greater line widths relative to the 294 K data.

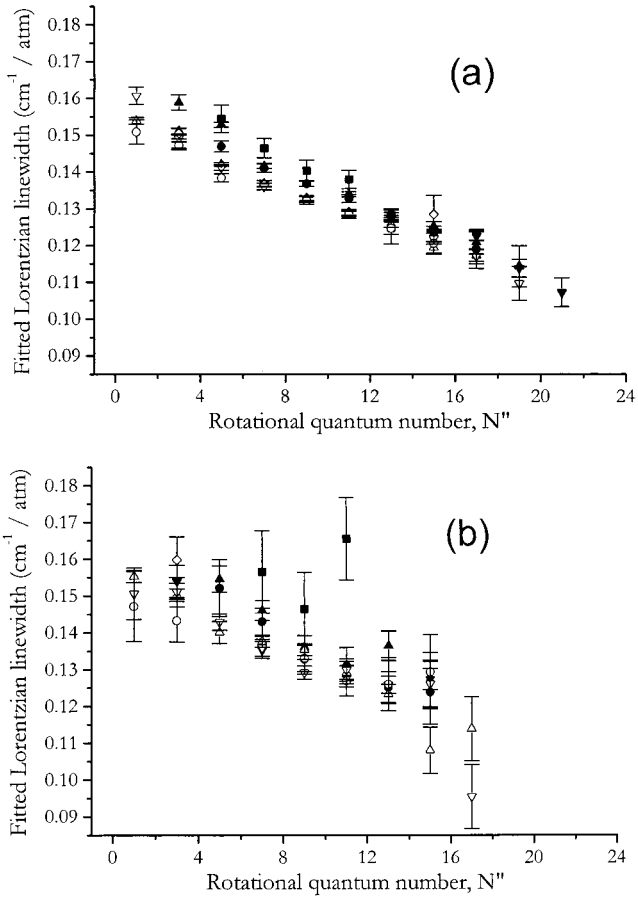

Figure 7. Graphs displaying fitted line widths for (a) pure O_2 and (b) zero air at 200 K. All values have been scaled to 1 atm unit pressure. Data points with relative errors greater than 5% in (a) and 10% in (b) have been excluded from the graphs. Symbols used to denote spectroscopic branches are the same as in Figure 5. Note the trend of increasing line width as the temperature is reduced, relative to the previous figures.

branch; for any given ground-state quantum number N'', the largest line widths are observed for the ^{O}P branch (notation $^{\Delta N}\Delta J$), with narrower widths for the ^{P}P and ^{P}Q branches, and the smallest widths for the ^{R}Q, ^{R}R, and ^{S}R branches. Thus, for a given N'', lines terminating at lower N' exhibit greater line widths than lines which terminate at higher N'. Shifting the ^{O}P line widths to $N'' - 4$ from N'', and ^{P}P, ^{P}Q line widths to $N'' - 2$ from N'' bunches these data much better. For these three branches, this is equivalent to plotting line widths versus N' rather than N'', and for such a plot although there is then agreement between the ^{O}P, ^{P}P, and ^{P}Q line widths, the values for the other branches diverge from them. Hence the branch dependence to the line width does not appear to bear a simple relationship to a single quantum number.

4.1.1. Dependence of Line Widths on Gas Composition. The pressure-normalized Lorentzian widths of a given rotational line from pure O_2 and O_2/N_2 mixtures might be expected to differ because the intermolecular forces and energy level structure of the colliding molecules are altered when nitrogen is introduced. To quantify this difference, average *pressure-normalized* line width data were compared by a simple fraction, whereby the increase/decrease in broadening is expressed as the ratio

$$R_{\gamma,\mathrm{air}} = \frac{\gamma_{\mathrm{air}}}{\gamma_{\mathrm{O_2}}} \tag{3}$$

Ratios for each temperature studied are plotted as a function of N'' in Figure 8. An error cutoff of 10% has been applied to remove spurious values, and a weighted least-squares fit ($\propto 1/\sigma^2$) to all remaining data points has been carried out to derive an average line width ratio factor, $\bar{R}_{\gamma,\mathrm{air}}$. Since any N dependence to these values is masked by data point uncertainties, the straight-line fits have been constrained to zero slope versus N''. Although it is perhaps possible to discern a slight decrease in $\bar{R}_{\gamma,\mathrm{air}}$ with N'', the trend cannot be quantified and must await more sensitive measurements. The $\bar{R}_{\gamma,\mathrm{air}}$ values obtained at 294, 243, and 200 K, respectively are 1.000 ± 0.012, 1.012 ± 0.006, and 1.002 ± 0.005 (all errors are 1σ).

Figure 8 demonstrates that the line broadening coefficients of O_2 $a^1\Delta_g - X^3\Sigma_g^-$ (0,0) lines by pure O_2 and 79% N_2 gas mixtures are indistinguishable within the uncertainty of the measurements presented here. Indeed, the results suggest that the mean ratio $\bar{R}_{\gamma,\mathrm{air}}$ differs from unity by $\leq 1\%$ over a wide temperature and quantum number range.

4.1.2. Dependence of Line Widths on Temperature. For a given quantum state, the Lorentzian pressure-induced line width increases as the temperature is reduced. To investigate these trends, the variation of γ with T was expressed as the ratio

$$R_{\gamma,\mathrm{T}} = \frac{\gamma_T}{\gamma_{T^*}} \tag{4}$$

where T^* is a reference temperature (chosen as ambient room temperature, 294 K). Figure 9 shows plots of γ_T/γ_{294} versus N''

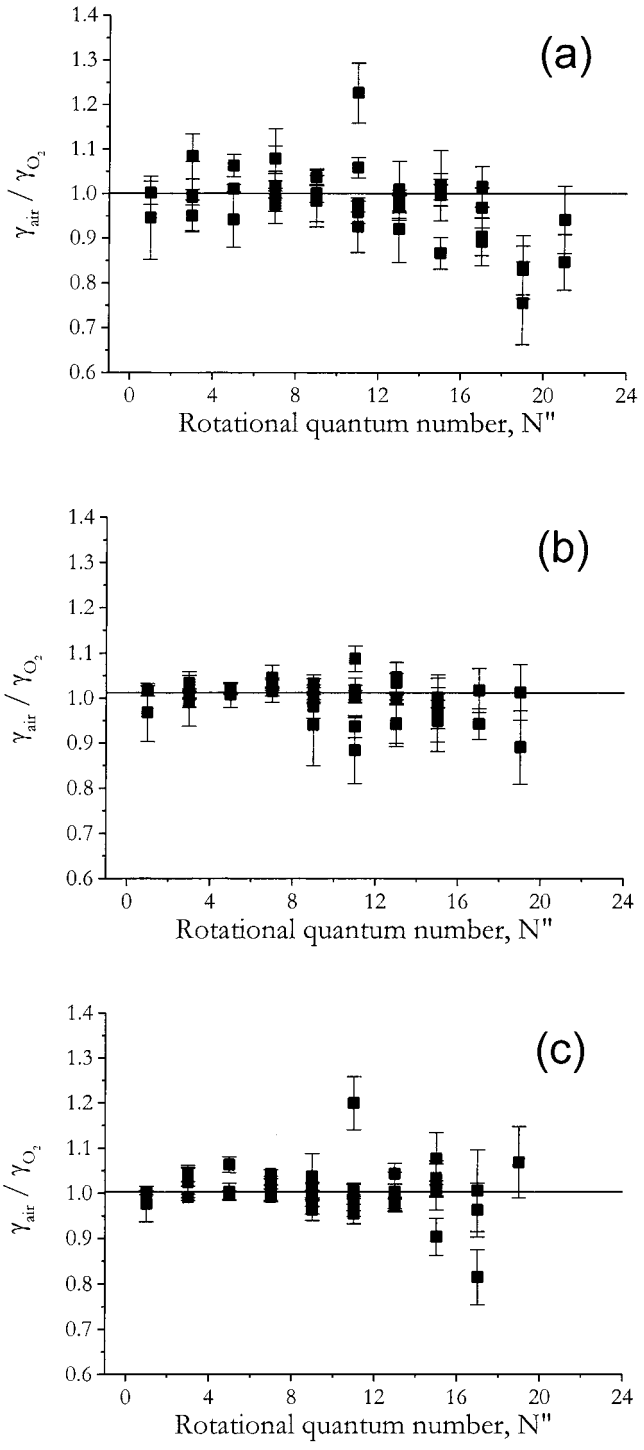

Figure 8. Ratio of individual line widths, $\gamma_{air}/\gamma_{O_2}$, plotted versus rotational quantum number. All values falling within a 10% relative error cutoff are included. (a) $T = 294$ K; (b) $T = 243$ K; (c) $T = 200$ K. Weighted least-squares fits to the data return average $\bar{R}_{\gamma,air}$ values of 1.000 ± 0.012, 1.012 ± 0.006, and 1.002 ± 0.005 (1σ errors), respectively, for the three temperatures.

for O_2 at $T = 243$ and 200 K; the graphs for zero air show identical behavior but with larger standard errors. Once again an error cutoff of 10% has been applied to remove spurious values, and a weighted least-squares fit to all remaining data points has been performed to derive an average T-dependent line width factor, $\bar{R}_{\gamma,T}$. The straight-line fits have been constrained to zero slope versus N'' as, again, no clear and quantifiable rotational dependence was found. The $\bar{R}_{\gamma,T}$ values for 243 and 200 K are 1.159 ± 0.014 and 1.394 ± 0.005 (1σ errors), respectively.

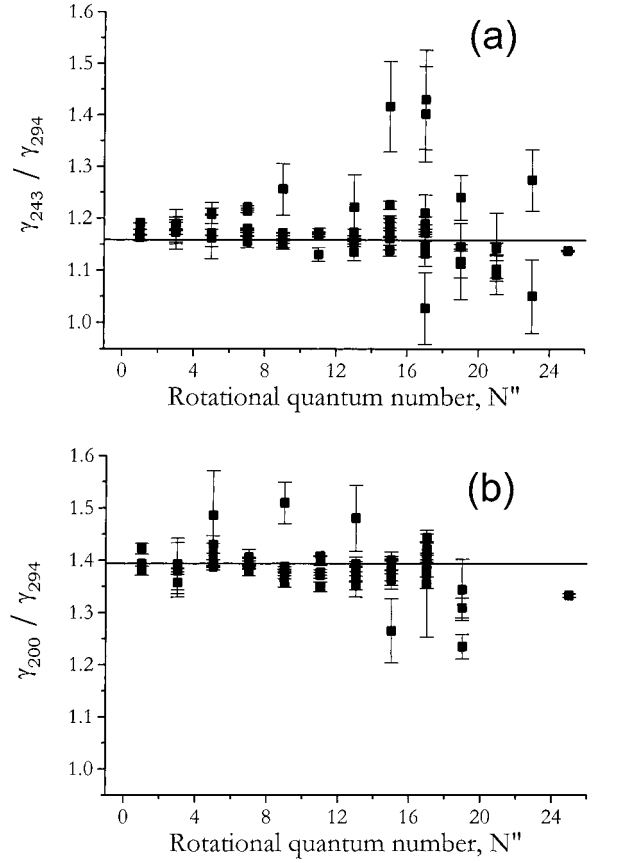

Figure 9. Ratio of individual line widths, γ_T/γ_{294K}, calculated for (a) $T = 243$ K; (b) $T = 200$ K. All values falling within a 10% relative error cutoff are included. Weighted least-squares fits to the data return average $\bar{R}_{\gamma,T}$ values of 1.159 ± 0.014 and 1.394 ± 0.005 (1σ errors), respectively.

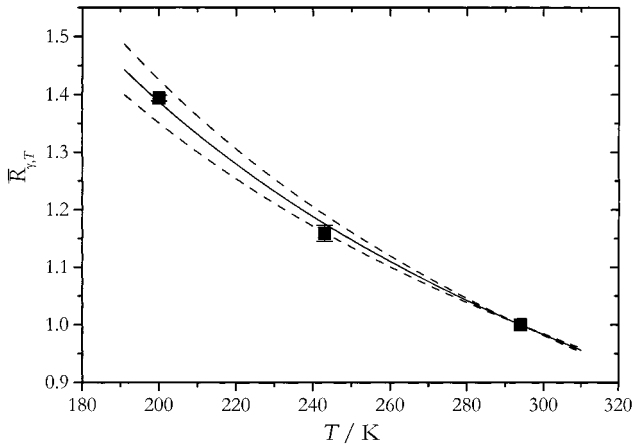

Figure 10. Average line widths $\bar{R}_{\gamma,T}$, expressed as ratios relative to 294 K, plotted as a function of temperature; by definition, the ratio at 294 K is unity. A least-squares fit of the data to the function $\bar{R}_{\gamma,T} = (T/294\text{ K})^n$ (solid line) shows the best agreement for $n = -0.85$. An estimated 8% error in this value, chosen to encompass all values, is represented by the dashed lines, which correspond to $n = -0.78$ and -0.92.

The mean temperature-dependent width factors $\bar{R}_{\gamma,T}$ are plotted in Figure 10. The data points were fitted to a function of the form

$$\bar{R}_{\gamma,T} = \left(\frac{T}{T^*}\right)^n \tag{5}$$

as applied by several authors (see, for example, ref 44) to

determine the temperature dependence of broadening coefficients. Note that the least-squares fit to only three data points is statistically robust here because the points themselves are weighted averages of a much larger number of independent values, with correspondingly small errors. The fit returned an index of $n = -0.85 \pm 0.07$, where the quoted error in the index encompasses the range of values required to span the data points as shown in Figure 10. The *T*-dependent line widths can thus be parametrized as $\gamma_T = \gamma_{294K}(T/294\ \mathrm{K})^{-0.85}$.

4.2. Spectral Line Shifts. Although the rotational line center wavenumbers were determined to high precision in the Voigt profile fits (to better than $\pm$ 0.001 cm^{-1}), no systematic line shifts as a function of pressure or temperature were noted. In part, the analysis was hindered by a spectrometer recalibration made between some measurements which precluded any very small shifts from being determined with confidence. Rotational line shifts to both the red and the blue ends of the electromagnetic spectrum have previously been observed in O_2 (in the b−X and Schumann Runge bands, respectively) but appear not be significant in the O_2 $a^1\Delta_g - X^3\Sigma_g^-$ (0,0) band. Line center wavenumbers derived from the Voigt profile fits for all experimental conditions are available in ref 41 or from the authors for all measured a−X (0,0) rotational lines.

4.3. Line Intensities. Integrated intensities (or cross sections) for each unblended rotational line were calculated directly from Voigt profile fits to the line shape, or can be derived by numerical integration across spectral lines. These values are tabulated in full in ref 41 and constitute a more comprehensive survey than previous determinations.[30,33,35] As was the case for the line widths, it is necessary to check that the integrated line intensities scale linearly with pressure. Figure 11 shows measured transition intensities for a selection of rotational lines at 294 K, plotted versus pressure, and demonstrates the linear relationship. The theoretical strength of each line is given by the slope of the straight line fit, having units cm^{-2} $Torr^{-1}$ or cm^{-2} atm^{-1}. In practice, rather than determining slopes of graphs for each rotational line, the equivalent procedure of dividing line intensities by pressure and taking a weighted average of the results was used. In order that measurements for different temperatures could be compared directly, the final results were scaled to molecular concentration, giving line intensity units of cm $molecule^{-1}$.

The integrated line intensities are given in a general form by the relation[29,45]

$$I_{J'J''} = \frac{\bar{\nu}}{4\pi\epsilon_0}\frac{8\pi^3 I_a C}{3hc}\frac{g'' e^{-F(J'')/kT}}{Q(T)}\left[1 - \exp\left(-\frac{hc\bar{\nu}}{kT}\right)\right]|\mathbf{R}|^2 \quad (6)$$

where $I_{J'J''}$ is in units of cm $molecule^{-1}$. $\bar{\nu}$ is the transition wavenumber (in cm^{-1}), I_a is the isotopic abundance of the species in question, *C* is the number density of the molecular species (in molecules cm^{-3}), g'' is the lower state degeneracy, the first exponential term contains the Boltzmann factor for the rotational energy level $F(J'')$, $Q(T)$ is the internal partition sum, and **R** is the transition dipole moment. We make the approximation that the electronic and vibrational (Franck−Condon) parts of **R** ($\mathbf{R}_{ev}$) are constant for a given vibronic band, with the rotational line-dependent part given by the Hönl-London factors,[46] $S_{J'',\Delta J}^{N'',\Delta N}$, for the transition: $|\mathbf{R}|^2 = S_{J'',\Delta J}^{N'',\Delta N}|\mathbf{R}_{ev}|^2$.[45]

The program PGOPHER computes relative line intensities, with due account of changes in the Boltzmann factor with temperature. The program computes Hönl-London factors by expansion of the rotational and electronic angular momentum parts of the molecular wavefuntion in a Hund's case (a) basis and thus makes no approximations for limiting case (a) or (b) behavior. Note that although the partition function in eq 6 is temperature dependent, relative intensities are unaffected at a single temperature. As pointed out by Gamache et al.[29] and Lafferty et al.,[33] a knowledge of relative intensities for individual *lines* allows the integrated *band* intensity to be determined. If the theoretical (fractional) contribution of a line to the overall band intensity is *f*, and the measured integrated line intensity is s_{int}, then the integrated AI for the entire band is

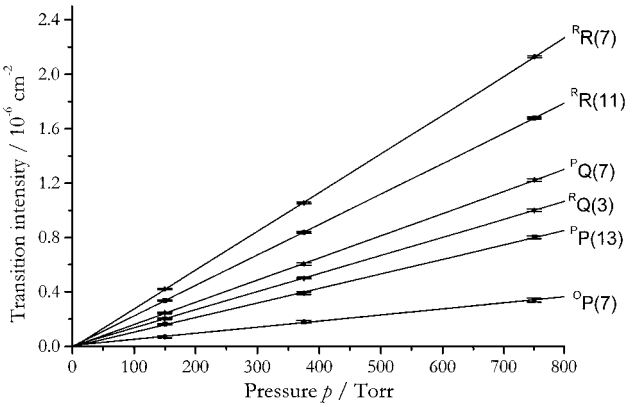

Figure 11. Transition intensities measured for six distinct rotational lines at three separate pressures at 294 K. The straight line fits for each transition have not been constrained to the graph origin, but nonetheless coincide closely with it.

$$S_{int} = \frac{s_{int}}{f} \quad (7)$$

Table 2 lists computed fractional line intensities and, for all rotational lines with sufficient signal-to-noise to warrant a quantitative analysis, gives band S_{int} values calculated from eq 7.

Although the S_{int} values inferred from individual line intensities show considerable variations (as should be expected for values derived from line intensities with relatively large errors) the average of the many determinations in Table 2 provides a reliable estimate of S_{int}. Table 3 brings together the error-weighted average of the band strengths from individual line intensities and compares the values with those determined from simple integration of the spectral intensity across the O_2 $a^1\Delta_g - X^3\Sigma_g^-$ (0,0) band performed as described in our previous paper.[34] The close correspondence of the numbers derived from the two analysis methods justifies approximations such as the invariance of the electronic and vibrational parts of the transition moment with rotational quantum number. Grand weighted averages of the S_{int} values from all experimental conditions for both methods used are also derived and are presented in Table 3 with corresponding Einstein *A* and *B* coefficients.

It is apparent from Table 3 that there is a small but quantifiable discrepancy between the values determined by the two integration procedures; S_{int} is consistently found to be larger when calculated using individual fractional line intensities than when numerical integration of the whole absorption band is used. In addition, the standard errors of the mean S_{int} values, propagated in the usual way, are not mutually inclusive of the discrepancy between the values. This suggests a significant (3−4%) systematic error in one or both of the methods used to determine the integrated band intensities. The most likely explanation is an unforeseen neglect of small absorbances in the numerical integrations of the band contours, such as the long tails of Lorentzian absorption lines, resulting in band strengths that are too small. The statistical averaging of numbers

TABLE 2: Integrated Band Strengths S_{int} (10^{-24} cm molecule^{-1}) Determined from Individual Line Intensities for a Range of Temperatures and Gas Mixtures[a]

			294 K				243 K				200 K			
$^{\Delta N}\Delta J$	J''	N''	$I_{J'J''}$	f	S_{int} (O_2)	S_{int} (air)	$I_{J'J''}$	f	S_{int} (O_2)	S_{int} (air)	$I_{J'J''}$	f	S_{int} (O_2)	S_{int} (air)
^{O}P	18	19	91.303	0.00187	3.848		52.018	0.00129	3.968		25.902	0.00079		
^{O}P	16	17	133.48	0.00273	3.421		84.809	0.00211	3.468		48.34	0.00147	3.943	
^{O}P	14	15	180.43	0.00370	3.194		126.35	0.00314	3.553	4.745	81.25	0.00247	3.143	3.503
^{O}P	12	13	223.57	0.00458	3.102		170.54	0.00424	3.240	2.666	121.93	0.00370	3.048	3.085
^{O}P	10	11	250.26	0.00513			205.53	0.00511	3.267	2.659	161.01	0.00489	3.287	3.839
^{O}P	8	9	246.21	0.00504	3.030		215.13	0.00535	3.143	2.916	181.99	0.00552	3.267	3.212
^{O}P	6	7	199.9	0.00409	3.414	3.955	183.66	0.00457	3.412	5.078	165.35	0.00502	3.239	3.467
^{O}P	4	5	109.39	0.00224	2.920		104.44	0.00260	3.000		98.61	0.00299	3.262	4.969
^{P}P	25	25	39.432	0.00081			15.071	0.00037	3.766		4.5756	0.00014		
^{P}P	23	23	71.28	0.00146	2.647		31.467	0.00078			11.422	0.00035		
^{P}P	21	21	120.68	0.00247	3.195		60.822	0.00151	3.134		26.015	0.00079		
^{P}P	19	19	190.93	0.00391	3.160		108.57	0.00270	3.260	5.982	53.936	0.00164	2.689	
^{P}P	17	17	281.34	0.00576	3.177		178.41	0.00444	3.363	3.354	101.45	0.00308	3.190	3.247
^{P}P	15	15	384.35	0.00787	3.154	3.293	268.64	0.00668	3.128	3.125	172.33	0.00523	3.137	3.298
^{P}P	13	13	483.42	0.00990	3.300	2.828	368.05	0.00915	3.201	2.993	262.51	0.00797	3.185	3.096
^{P}P	11	11	553.54	0.01134	3.314	3.091	453.69	0.01128	3.194	3.525	354.56	0.01076	3.215	3.016
^{P}P	9	9	565.54	0.01158	3.276	3.068	493.17	0.01227	3.247	3.013	416.18	0.01263	3.227	3.002
^{P}P	7	7	494.73	0.01013	3.264	3.215	453.62	0.01128	3.217	3.105	407.37	0.01237	3.286	3.115
^{P}P	5	5	332.64	0.00681	3.055	2.918	316.93	0.00788	3.210	3.024	298.48	0.00906	3.225	3.157
^{P}P	3	3	104.87	0.00215			102.61	0.00255	3.369		99.873	0.00303	3.185	4.827
^{P}Q	22	23	80.905	0.00166	4.197		35.783	0.00089	2.740		13.018	0.00040		
^{P}Q	20	21	138.55	0.00284	2.901		69.959	0.00174	2.913		29.993	0.00091		
^{P}Q	18	19	222.25	0.00455			126.62	0.00315	3.423	3.997	63.051	0.00191	3.253	4.216
^{P}Q	16	17	333.14	0.00682	3.138	3.373	211.67	0.00526	3.107	2.893	120.65	0.00366	3.318	3.314
^{P}Q	14	15	465.11	0.00953	3.246	3.412	325.71	0.00810	3.211	2.951	209.45	0.00636	3.267	3.330
^{P}Q	12	13	601.91	0.01233	3.302	3.399	459.16	0.01142	3.253	3.396	328.28	0.00997	3.245	3.400
^{P}Q	10	11	716.67	0.01468	3.234	3.768	588.56	0.01464	3.252	3.278	461.09	0.01400	3.263	3.037
^{P}Q	8	9	775.1	0.01588	3.295	3.229	677.25	0.01685	3.234	3.253	572.95	0.01739	3.324	3.079
^{P}Q	6	7	742.47	0.01521	3.209	3.127	682.15	0.01697	3.236	3.315	614.15	0.01864	3.261	3.249
^{P}Q	4	5	590.69	0.01210	3.221	3.056	563.95	0.01403	3.198	3.251	532.49	0.01617	3.314	3.169
^{P}Q	2	3	285.13	0.00584	3.197	3.355	279.58	0.00695	3.298	3.050	272.85	0.00828	3.286	3.364
^{Q}Q	27	27	46.638	0.00096	3.553		15.254	0.00038			3.8179	0.00012		
^{Q}Q	23	23	166.18	0.00340			73.362	0.00182	3.081	2.520	26.628	0.00081		
^{Q}Q	21	21	285.55	0.00585	4.077	3.748	143.91	0.00358			61.553	0.00187	3.479	
^{Q}Q	19	19	459.92	0.00942	3.319	2.918	261.54	0.00651	3.304	2.908	129.92	0.00394	3.190	3.403
^{Q}Q	17	17	692.94	0.01419	3.220	3.290	439.43	0.01093	3.253	3.260	249.88	0.00759	3.310	3.231
^{Q}Q	15	15	973.82	0.01995	3.220	3.191	680.64	0.01693	3.245	3.275	436.63	0.01326	3.228	3.277
^{Q}Q	13	13	1271.4	0.02604	3.190	3.172	967.94	0.02408	3.166	3.160	690.37	0.02096	3.203	3.178
^{Q}Q	9	9	1688.6	0.03459	3.121		1472.5	0.03663			1242.6	0.03772		
^{Q}Q	7	7	1669.7	0.03420	3.220	3.193	1531	0.03808	3.261	3.336	1374.9	0.04174	3.248	3.198
^{Q}Q	3	3	917.62	0.01880	3.235	3.181	897.83	0.02233	3.314	3.238	873.89	0.02653	3.280	3.231
^{Q}R	20	21	81.816	0.00168			41.311	0.00103	3.414		17.711	0.00054		
^{Q}R	18	19	133.56	0.00274	3.276		76.096	0.00189	3.316		37.891	0.00115		
^{Q}R	16	17	204.6	0.00419	2.864		130	0.00323	3.361		74.096	0.00225	3.065	
^{Q}R	14	15	293.63	0.00601	3.190		205.62	0.00511	3.480		132.22	0.00401	3.554	
^{Q}R	8	9	573.18	0.01174	3.223		500.83	0.01246			423.7	0.01286		
^{Q}R	2	3	570.27	0.01168	3.307	2.965	559.16	0.01391	3.341	3.156	545.7	0.01657	3.342	3.236
^{Q}P	22	21	63.8	0.00131	2.917		32.225	0.00080			13.821	0.00042		
^{Q}P	20	19	101.49	0.00208	3.200		57.838	0.00144	2.914		28.811	0.00087		
^{Q}P	18	17	150.59	0.00308	3.347		95.707	0.00238	3.163		54.57	0.00166	2.692	
^{Q}P	14	13	264.49	0.00542	3.318		201.8	0.00502			144.31	0.00438	3.340	
^{Q}P	10	9	324.56	0.00665	3.311		283.62	0.00705			239.97	0.00729		
^{R}R	1	1	1012.6	0.02074	3.218	3.188	1005.5	0.02501	3.172	3.251	996.79	0.03026	3.253	3.223
^{R}R	3	3	1179.8	0.02417	3.217	3.152	1154.4	0.02871	3.204	3.217	1123.6	0.03411	3.229	3.107
^{R}R	5	5	1293.6	0.02650	3.234	3.204	1232.5	0.03066	3.274	3.196	1160.8	0.03524	3.225	3.233
^{R}R	7	7	1298.7	0.02660	3.212	3.123	1190.8	0.02962	3.300	3.220	1069.4	0.03246	3.228	3.208
^{R}R	9	9	1199.8	0.02458	3.242	3.274	1046.2	0.02602	3.225	3.191	882.91	0.02680	3.226	3.219
^{R}R	11	11	1026.1	0.02102	3.239	3.162	841.02	0.02092	3.269	3.216	657.26	0.01995	3.260	3.187
^{R}R	13	13	816.18	0.01672	3.227	3.181	621.4	0.01546	3.192	3.311	443.2	0.01345	3.230	3.139
^{R}R	15	15	605.84	0.01241	3.214	3.206	423.44	0.01053	3.213	3.231	271.64	0.00825	3.259	3.014
^{R}R	17	17	420.72	0.00862	3.219	3.018	266.8	0.00664	3.250	3.271	151.71	0.00461	3.309	3.255
^{R}R	21	21	167.34	0.00343	3.299	3.211	84.338	0.00210	3.210	2.764	36.074	0.00110	3.004	5.213
^{R}R	23	23	96.109	0.00197	3.414		42.428	0.00106	3.878		15.4	0.00047		
^{R}R	25	25	51.928	0.00106	3.454		19.847	0.00049			6.0256	0.00018		
^{R}R	27	27	26.417	0.00054	3.194		8.6404	0.00021			2.1626	0.00007		
^{R}R	29	29	12.663	0.00026	2.585		3.5032	0.00009			0.7125	0.00002		

TABLE 2 (Continued)

			294 K				243 K				200 K			
$^{\Delta N}\Delta J$	J''	N''	$I_{J'J''}$	f	S_{int} (O_2)	S_{int} (air)	$I_{J'J''}$	f	S_{int} (O_2)	S_{int} (air)	$I_{J'J''}$	f	S_{int} (O_2)	S_{int} (air)
^{R}Q	2	1	262.15	0.00537	3.177	3.439	260.82	0.00649	3.188	3.585	259.17	0.00787	3.328	2.903
^{R}Q	4	3	616.18	0.01262	3.218	3.017	604.1	0.01503	3.312	3.296	589.45	0.01789	3.244	3.227
^{R}Q	6	5	841.25	0.01723	3.230	3.393	803.16	0.01998	3.253	3.256	758.33	0.02302	3.285	3.182
^{R}Q	8	7	942.08	0.01930	3.217	3.291	865.58	0.02153	3.261	3.331	779.33	0.02366	3.275	3.146
^{R}Q	10	9	929.44	0.01904	3.250	3.189	812.19	0.02020	3.254	3.182	687.19	0.02086	3.247	3.117
^{R}Q	12	11	830.61	0.01701	3.196	3.307	682.23	0.01697	3.196	3.188	534.57	0.01623	3.231	3.191
^{R}Q	14	13	681.81	0.01397		3.306	520.2	0.01294		3.409	372.01	0.01129		
^{R}Q	16	15	518.22	0.01061	3.178	3.374	362.99	0.00903	3.205	3.163	233.48	0.00709	3.200	3.299
^{R}Q	18	17	366.58	0.00751	3.192	3.171	232.97	0.00579	3.292	3.181	132.84	0.00403	3.259	2.815
^{R}Q	20	19	242.18	0.00496	3.201	2.961	138.02	0.00343	3.076	2.605	68.75	0.00209	3.111	2.907
^{R}Q	22	21	149.79	0.00307	3.200	3.439	75.659	0.00188	3.252	3.390	32.45	0.00099	3.109	
^{R}Q	24	23	86.905	0.00178	3.384		38.451	0.00096	3.142		13.995	0.00042		
^{R}Q	26	25	47.361	0.00097	3.009		18.143	0.00045			5.5235	0.00017		
^{R}Q	28	27	24.273	0.00050	3.223		7.957	0.00020			1.9972	0.00006		
^{S}R	2	1	524.31	0.01074	3.307	3.123	521.64	0.01297	3.370	3.236	518.34	0.01574	3.315	3.071
^{S}R	4	3	639	0.01309	3.259	3.349	626.47	0.01558	3.336	3.258	611.29	0.01856	3.289	3.164
^{S}R	6	5	698.89	0.01432		3.563	667.24	0.01660		3.246	630	0.01913	3.394	
^{S}R	10	9	639.3	0.01309	3.260	3.305	558.65	0.01390	3.214	3.217	472.67	0.01435	3.249	3.243
^{S}R	12	11	543.68	0.01114	3.270	3.180	446.55	0.01111	3.269	3.079	349.9	0.01062	3.224	3.092
^{S}R	14	13	430.43	0.00882	3.262	3.173	328.41	0.00817	3.276	3.024	234.85	0.00713	3.237	3.226
^{S}R	16	15	318.26	0.00652	3.261	2.955	222.93	0.00554	3.346	3.307	143.39	0.00435	3.238	3.515
^{S}R	18	17	220.3	0.00451	3.231	2.890	140.01	0.00348	3.162	5.115	79.828	0.00242	3.068	3.769
^{S}R	20	19	143.01	0.00293	3.394	3.341	81.5	0.00203	3.288		40.597	0.00123	3.679	
^{S}R	22	21	87.181	0.00179	3.155	2.846	44.035	0.00110	3.169		18.887	0.00057		
^{S}R	24	23	49.969	0.00102	3.225		22.109	0.00055			8.0471	0.00024		
^{S}R	26	25	26.951	0.00055	2.675		10.324	0.00026			3.1432	0.00010		

[a] The branch labels and rotational quantum numbers for the lines studied appear on the left. $I_{J'J''}$ is the computed rotational line strength (from PGOPHER,[38] arbitrary units) at the specified temperature. f is the fractional contribution of this intensity to the total band intensity (determined by summing all theoretical intensities for $J \leqslant 100$). Integrated line intensities measured for O_2 and zero air have been divided by the respective f values to derive S_{int} values for each rotational line.

TABLE 3: Results for Integrated Band Strengths of $^{16}O_2$ $a^1\Delta_g - X^3\Sigma_g^-$ (0,0) Spectra Recorded under Various Experimental Conditions, Determined by Two Complementary Methods[a]

		$S_{int}/10^{-24}$ cm molecule^{-1}	
	concn of O_2/ mol m^{-3}	from individual line strengths	from band integration
100% O_2, 294 K	40.907(70)	3.211(18)	3.119(31)
	20.458(68)		3.119(46)
	8.175(29)		3.123(98)
21% O_2/79% N_2, 294 K	8.597(31)	3.177(58)	3.167(94)
	4.300(14)		3.14(14)
	1.720(05)		3.16(21)
100% O_2, 243 K	49.496(86)	3.207(31)	3.007(48)
	10.247(38)		3.15(11)
21% O_2/79% N_2, 243 K	10.395(22)	3.176(71)	3.03(12)
	2.067(17)		3.13(18)
100% O_2, 200 K	30.32(11)	3.232(38)	3.086(56)
	12.146(42)		3.23(12)
21% O_2/79% N_2, 200 K	12.47(11)	3.21(14)	2.86(19)
	2.430(13)		3.19(24)
av S_{int}		3.210(15)	3.091(43)
Einstein B coeff (cm^2 erg^{-1} s^{-1})		0.06145(28)	0.05918(82)
Einstein A coeff (10^{-4} s^{-1})		2.256(10)	2.173(31)

[a] For S_{Int} values calculated from fractional line strengths, weighted averages of the data in Table 2 (with propagated errors) are presented for each gas mixture and temperature studied. Also presented are the results for numerical integrations of complete band contours; since these results were not pressure scaled they are displayed as a function of gas concentration as well as composition and temperature. The minor systematic differences between values derived from the two methods are discussed in the text. Quoted errors represent one standard deviation, taking into account all known sources of uncertainty.

used to generate S_{int} values from isolated line intensities should remove systematic errors for that case. It should be noted that no significant differences arise in measured values of S_{int} for different gas compositions, pressures or temperatures. The Einstein coefficients for the O_2 $a^1\Delta_g - X^3\Sigma_g^-$ (0,0) transition are thus observed to be invariant to these parameters over the range of conditions studied.

5. Discussion

5.1. Line Widths. The broadening of spectral lines by homogeneous processes gives rise to Lorentzian line shapes, and the width of each line is inversely related to the lifetimes of the molecular states involved in the transition. If the spectral broadening is caused by collisions between molecules then the average time between collisions may be approximately equated with the lifetime of a state; i.e., the degree of pressure broadening is a measure of the rate of change of rotational quantum numbers. A more rigorous theoretical prediction of line broadening and line shift parameters for particular molecular systems is a problem of substantial computational complexity. Anderson theory[47,48] has been used to calculate pressure broadening coefficients for many molecular systems, most successfully for linear molecules[1,49,50] where the intermolecular potential is well-known. Alternatively, the theory may be used to infer unknown multipole moments from accurate spectroscopic measurements.[49]

The N dependence of the Lorentzian line widths presented in section 4.1 is the most comprehensive quantitative analysis carried out on the O_2 a−X (0,0) band system. Many previous authors have assumed a constant N-independent value for the pressure broadening widths, though Lafferty et al.[33] did ascribe a quadratic function (to a noisier data set than those presented here) of the form

$$\gamma = \gamma_0 + {}^1/_2\Delta_\gamma[N''(N''+1) + N'(N'+1) - 4] \qquad (8)$$

where γ_0 and Δ_γ are fitted constants. Although this formula

allows for differential broadening of lines with the same N'' but from different branches, it fails to reproduce the magnitudes or trends of the observed room-temperature line widths from the current study using the preferred fitted constants of ref 33. The N dependence to the line widths extracted from our data and exhibited in Figures 5−7 is not well represented by a quadratic formula like eq 8.

Line widths in the (2,0), (1,0), and (0,0) bands of the O_2 $b^1\Sigma_g^+ - X^3\Sigma_g^-$ transition have been more thoroughly investigated due to the greater strength of this electronic transition. In all cases, a similar trend of decreasing line width with increasing N'' was observed, with line width magnitudes for a given N'' depending upon the rotational branch. For the b−X (0,0) band (the so-called A band) a systematic difference of measured rotational line widths was found between branches[40] (line widths of ^{P}P and ^{P}Q transitions exceed those for the ^{R}R and ^{R}Q transitions involving a common N'') though a very recent study reported no differences.[51] fwhm Lorentzian line widths in the b−X (0,0) band lie in the range 0.11 cm^{-1} atm^{-1} for $N'' = 1$ to 0.07 cm^{-1} atm^{-1} for $N'' = 29$ at 296 K and thus are comparable to those in the a−X (0,0) band at room temperature. Because of a lack of data for the a−X system, the A band values were used in the previous HITRAN database[31] to describe the broadening of a−X rotational lines.

Line width values for the b−X (1,0) band[52] (the B band) are approximately 10% greater than for the b−X (0,0) band, but show the same rotation-dependent trend. Values for the b−X (2,0) band[53] (γ band) concur with those from the A band, but show larger variations as a function of N''. Pressure-broadened widths for rotational lines in the predissociated Schumann−Runge ($B^3\Sigma_u^- - X^3\Sigma_g^-$) system of O_2 have been investigated for pressures of 10−60 atm.[48] In contrast to other O_2 bands, no significant dependence of line width on rotational quantum number was observed, with fwhm remaining constant at around 0.2 cm^{-1} atm^{-1}.

Amano et al.[55] probed the pure rotation $N = 7 \leftarrow 6$ transition within the O_2 ($a^1\Delta_g$) $v = 0$ manifold by submillimeter-wave spectroscopy and deduced a fwhm pressure-broadening coefficient of ∼0.10 cm^{-1} atm^{-1}. Both self-broadening and N_2-broadening effects were investigated, with little difference in magnitudes observed between the two gas mixtures. The authors noted that, to a good approximation, the pressure broadening of a rotational line in an electronic transition can be taken as the mean of the values for the upper and lower states. The pure rotation ground state $X^3\Sigma_g^-$ $N = 7 \leftarrow 6$ line is broadened by 0.108 cm^{-1} atm^{-1} (fwhm).[56] A simple average of the $a^1\Delta_g$ and $X^3\Sigma_g^-$ values implies rotational line widths in the same N range of ∼0.104 cm^{-1} atm^{-1} for the O_2 a−X (0,0) band. This compares favorably with the results presented herein (e.g., ^{Q}Q($N = 7 \leftarrow 7$) has width 0.098 cm^{-1} atm^{-1}, ^{P}Q($N = 6 \leftarrow 6$) has width 0.101 cm^{-1} atm^{-1}, for O_2 at 294 K).

A qualitative explanation for the general trend of decreasing line width with N is obtained from energy transfer arguments. For rotation-changing collisions, the bigger the translational energy change the less likely the relaxation or excitation process becomes. Hence the most efficient collisions will involve exactly resonant rotational-to-rotational energy transfer. The rate of collisional energy transfer (and hence the contribution to broadening) will thus be greatest for the most populated N levels, i.e., will coincide with the peak of the Boltzmann distribution. If this effect were to dominate, the plots of γ versus rotational angular momentum would exhibit a peak at $N \approx 8$ at room temperature. In fact the line widths decrease monotonically with N, suggesting that resonant collisions are not the only contributors to the line widths (at least at the lowest values of N which exhibit the largest widths). Since the energy spacing between consecutive rotational levels is approximately proportional to N, nonresonant N-changing collisions will be most efficient at low N since the translational energy release or gain is minimized. Thus, as collisions preferentially relax or excite molecules with small angular momenta, the measured line widths are greatest in any given branch for minimum N. This interpretation has also recently been proposed in a study of line broadening of the O_2 b−X (0,0) band[57] to account for the similar rotational state dependence of the line width in this band.

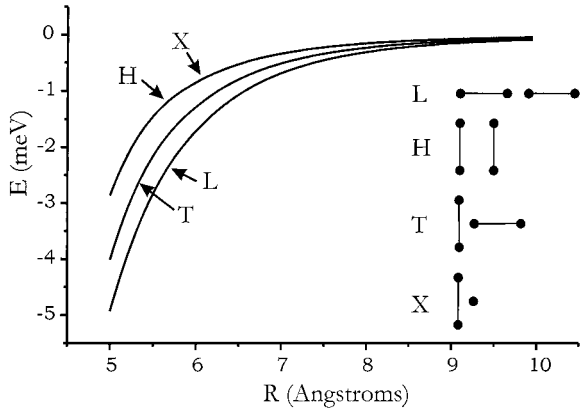

Figure 12. Ab initio long-range potentials (adapted from refs 58,59) for four orientations of the $O_2(X^3\Sigma_g^-) - O_2(X^3\Sigma_g^-)$ system, plotted as functions of the center-of-mass separations. The H and X geometries produce indistinguishable potential curves. A significant well extends out to large (∼10 Å) separation and is approximately 12 meV (100 cm^{-1}) deep at the potential minimum.

An important factor in collisionally induced rotational transitions will be the anisotropy of the intermolecular potential, because rotational transitions may only be induced by an angular dependence to the interaction. The typical intermolecular distance characterizing a collision may be crudely estimated using the hard sphere gas kinetic model. The collision frequency at 1 atm pressure and 294 K is approximately $z = 1.53 \times 10^{28}$ m^2 s^{-1} $\times$ σ, where σ is the collision cross-section. A typical value for pressure broadening in the O_2 a−X (0,0) band is 0.10 cm^{-1} at 1 atm and 294 K. Assuming the Lorentzian width is inversely proportional to the molecular state lifetime τ, values of $\tau = 5.3 \times 10^{-11}$ s and $z = 1/\tau = 1.9 \times 10^{10}$ s^{-1} are implied. Hence an effective cross-section $\sigma = 1.2 \times 10^{-18}$ m^2 may be derived. This corresponds to a hard-sphere center-to-center collision distance of ∼6.3 Å, and the extended range of this interaction is consistent with the fact that we were unable to resolve any spectral lineshifts with increasing pressure because of the dominance of impact over van der Waals type broadening.

Figure 12 shows ab initio intermolecular potentials for four distinct geometries of $O_2(X^3\Sigma_g^-) - O_2(X^3\Sigma_g^-)$ interactions.[58,59] The long-range part of the potential is shown to emphasize the extent of the attractive well, which is significant at large internuclear separations. The anisotropy of the potentials is evident from the variation for the various geometries for approaches closer than 10 Å. Further ab initio studies[60] of the O_2-O_2 system have also concluded that significant angular anisotropy is present in both $O_2(a^1\Delta_g) - O_2(a^1\Delta_g)$ and $O_2(X^3\Sigma_g^-) - O_2(a^1\Delta_g)$ dimer potentials at long range.

The almost exact equivalence of line widths measured from spectra of pure O_2 and O_2/N_2 mixtures implies that the addition of molecular nitrogen as a collision partner makes no difference to the O_2 a−X line broadening efficiency when compared with self-broadening at all temperatures studied. This is probably in

large part due to the similarity of the intermolecular forces in the O_2-O_2 and O_2-N_2 systems, although the latter have not been the subject of ab initio calculations so quantitative comparisons cannot be made. Both O_2 and N_2 lack a dipole moment, and consequently weaker quadrupole and dispersion interactions are expected to dominate the intermolecular interaction potentials, so the O_2-O_2 and O_2-N_2 potentials should have a similar form, anisotropy, and range.

Differences between O_2- and N_2-broadened widths have been observed for rotational transitions in other O_2 bands. Several lines of the A band have been subjected to analysis with O_2,[61] N_2,[62] and He[63] as collision partners. These studies revealed N_2-broadening coefficients ~70% greater than for the self-broadening case, while the He-broadened widths were ~25% smaller. More comprehensive studies of line-broadening in the A band, however, showed very similar line widths for pure O_2 and for O_2 diluted in N_2 (differing at most by ~3%).[40,51] The effect of N_2 interactions on the O_2 b−X (1,0) band has also been investigated by CRDS.[64] N_2-broadening was found to exceed self-broadening by around 12% implying slightly different intermolecular interaction potentials.

The temperature dependence of the (average) broadening coefficients, as represented by the index n in eq 5, is best described by $n = -0.85 \pm 0.07$, which is judged to be approximately rotation-independent. This analysis demonstrates a broadly similar decrease in line width with temperature in the O_2 $a^1\Delta_g - X^3\Sigma_g^-$ (0,0) band system as is observed for other molecules.[44,65−68] The simplest starting point for consideration of the temperature dependence of spectral line broadening is once again the kinetic theory of gases which predicts a collision frequency for each molecule $z \propto pT^{-0.5}$. Since the line width results presented here have been normalized to unit pressure, the exponent n would be expected to be close to −0.5 if the molecules behave as hard spheres. Any real molecular system will depart from the hard sphere model due to interactions via the intermolecular potential energy surface. A simple model for the variation of line width with temperature, taking account of terms in the interaction potential,[49] predicts that individual line widths will conform approximately to the relation

$$\gamma(T) \propto T^{-(q+1)/(2(q-1))} \tag{9}$$

for a predominant interaction potential of the form r^{-q}. Thus, for dipole−dipole interactions ($q = 3$) the index $n \approx -1$, for quadrupole−quadrupole terms ($q = 5$) dominating $n \approx -0.75$, and for dispersion forces ($q = 6$) $n \approx -0.70$. The expectation that a quadrupole−quadrupole interaction will dominate the O_2-O_2 and O_2-N_2 potentials is therefore in broad agreement with the experimentally determined value of $n \approx -0.85$.

A high-resolution study of the O_2 b−X A band obtained improved Einstein coefficients and line widths at 296 and 198 K.[45] These results were analyzed to derive an exponent for the temperature dependence of the line width of $n = -0.674(8)$. More recently, exponents for the A band that change with increasing N' from −0.77 to −0.60 have been reported.[51] These values differ somewhat from the present determination, but it remains unclear how far parallels should be drawn between different electronic bands.

5.2. Line Intensities. A major accomplishment from this study of O_2 $a^1\Delta_g - X^3\Sigma_g^-$ (0,0) line intensities is improved integrated band absorption intensity values and Einstein coefficients (see Table 3). The findings that the absorption intensities are straightforwardly proportional to gas concentration have been questioned previously by Minaev, who invoked a mechanism for enhancing the a−X transition at higher pressures by collision complex formation. The a−X transition borrows intensity from the collision induced electric dipole b−a (Noxon) transition because of a component of $b^1\Sigma_g^+$ state character mixed into the ground $X^3\Sigma_g^-$ state.[69,70] We note, however, that the effect should be small for the (sub) atmosphere pressures used in this study, and will contribute most to an enhanced collision-induced O_2-O_2 dimer absorption underlying the a−X band; this is clearly detectable at higher pressures, but appears to be a distinct phenomenon from the highly structured O_2 monomer absorption.

TABLE 4: Integrated Absorption Intensities and Einstein *A* Coefficients for the $^{16}O_2$ $a^1\Delta_g - X^3\Sigma_g^-$ (0,0) Band[a]

exptl method	$S_{int}/10^{-24}$ cm molecule^{-1}	*A* coeff/ 10^{-4} s^{-1}	exptl conditions	ref
FTS	3.210(15)	2.256(10)	pure O_2 and 21%:79% O_2:N_2 mixtures; $T = 200-294$ K, $p = 140-750$ Torr	this work
FTS	3.11(7)	2.19(5)	pure O_2, $T = 298$ K	34
CRDS	3.05(10)	2.14(7)	pure O_2, $T = 298$ K	34
FTS	3.166(69)	2.225(51)	pure O_2, $T = 296$ K, $p = 98-780$ Torr	33
FTS	3.247(80)	2.28(5)	pure O_2, $T = 299$ K, $p = 98-795$ Torr	35

[a] Values reported in the table are those published from 1998 onward.

The integrated band absorption intensity values derived in this work are in good agreement with measurements by Lafferty et al.[33] who determined $S_{int} = 3.166(69) \times 10^{-24}$ cm molecule^{-1} from fractional line intensities for $^{16}O_2$, and with our values derived previously from FTS and CRDS.[34] A very recent study[35] of O_2 $a^1\Delta_g - X^3\Sigma_g^-$ (0,0) line parameters was performed by recording spectra of pure oxygen over a range of pressures (but not temperatures) with a 107 m path cell and FT spectrometer. The conclusions reached are largely the same as those contained herein, though the accuracy of the parameters obtained is less than in the current work, and quantum number dependent trends in line widths were not so clearly established. An integrated band absorption intensity of $S_{int} = 3.247(80) \times 10^{-24}$ cm molecule^{-1} was obtained from direct integration of the band contour, again supporting the results published from 1998 onward. These post-1998 S_{int} values and the associated Einstein A coefficients are summarized in Table 4. The individual line data from Brault and Brown,[30] which were reanalyzed by Gamache et al.[29] by the fractional intensity method, returned an average value $S_{int} = 3.69 \times 10^{-24}$ cm molecule^{-1}. This determination, and many of the others made over the past decade, lie far outside any sensible error estimate based on the most recent results discussed above.

The relative merits of the two alternative techniques used to derive integrated band intensities from absorption spectra deserve consideration. Numerical integration of the whole band is relatively straightforward to apply, and does not rely on the availability of unblended spectral lines. Furthermore, this method requires no prior knowledge of the theoretical forms for the line strength factors. However, the discrepancies between the data sets obtained by the two methods suggest that the integration process suffers from small systematic errors, most probably caused by difficulties in accurately specifying the zero absorption baseline. It may be possible to reduce these problems by careful measurements of baselines in vacuo before or after measurements. The use of ratios of integrated and fractional line intensities is more complex, requiring very many isolated line fits and theoretical band simulations. Nevertheless, it has the great advantage of providing a large number of statistically independent values which may be averaged to obtain a

satisfactorily small standard error. This lack of systematic bias makes the fractional intensity procedure more reliable in the current study, and hence the value $S_{int} = 3.210(15) \times 10^{-24}$ cm molecule^{-1} is recommended. With the very small fractional standard error in S_{int} (~0.5%), and therefore in the Einstein A and B coefficients, this determination represents a substantial improvement in the precision to which these parameters are known. In the past decade the recommended measurements have disagreed by more than 50%.

6. Summary

For accurate parametrization of the infrared airglow, and the determination of radiative transfer characteristics of the Earth's atmosphere, careful laboratory studies of the O_2 $a^1\Delta_g - X^3\Sigma_g^-$ (0,0) band are essential. The current study represents the most extensive survey of this transition to date, with analysis of rotational line positions, intensities and widths as functions of temperature (200 K $\leq T \leq$ 294 K), pressure (150 Torr $\leq p \leq$ 750 Torr) and gas composition (100% O_2 and 21% O_2: 79% N_2).

Rotational branch-dependent trends of decreasing line widths with increasing rotational quantum number, previously approximated in the HITRAN database by O_2 b−X (0,0) band parameters, have been determined accurately for the first time. Line widths are found to be effectively independent of gas composition (in direct contrast to other O_2 bands). These trends have been interpreted in terms of the quantum efficiency of bimolecular collisional energy transfer, and the dominance of quadrupole−quadrupole interactions in determining the intermolecular interaction potential. The temperature dependence of Lorentzian line widths is found to be well represented by the expression $\gamma_T = \gamma_{294K}(T/294\ K)^{-0.85}$, apparently independent of rotational quantum number.

No significant line shifts with increasing pressure were observed, suggesting that these effects are very minor. Individual integrated line intensities have been measured over a broad range of rotational quantum numbers. These were converted to integrated absorption intensities by division by their calculated respective fractional contributions to the whole band intensity, with a resultant average value of $S_{int} = 3.210(15) \times 10^{-24}$ cm molecule^{-1} for $^{16}O_2$. An alternative method of obtaining S_{int}, by direct numerical integration of band contours, results in a mean value of $3.091(43) \times 10^{-24}$ cm molecule^{-1}. Both procedures gave S_{int} values which were independent of pressure, temperature or gas composition. The method using individual line intensities is judged to be the more reliable, theoretically free from systematic error, and therefore the recommended values from this study for $^{16}O_2$ are

$$S_{int} = 3.210(15) \times 10^{-24}\ \text{cm molecule}^{-1}$$

$$B = 0.06145(28)\ \text{cm}^2\,\text{erg}^{-1}\text{s}^{-1}$$

$$A = 2.256(10) \times 10^{-4}\ \text{s}^{-1}$$

Derived values compare favorably with recent measurements by ourselves[34] and others,[33,35] which are summarized in Table 4. The effect of including other isotopes in their appropriate natural abundances and assuming comparable transition intensities, is to increase these values for O_2 in the terrestrial atmosphere, giving $S_{int} = 3.226(15) \times 10^{-24}$ cm molecule^{-1} from the current study (cf. $3.182(69) \times 10^{-24}$ cm molecule^{-1} from ref 33). This growing consensus greatly reduces the uncertainty in the integrated AI and Einstein coefficients which have been evident in the past decade. The information gathered in this study serves to increase the scope and accuracy of parameters describing the intensity of the O_2 $a^1\Delta_g - X^3\Sigma_g^-$ (0,0) transition and should remove inaccuracies relating to this transition from future atmospheric spectral databases.

Acknowledgment. We are grateful to U.K. Natural Environment Research Council (NERC) for funding for this work, the award of a postgraduate studentship to S.M.N. (NERC ref. GST/02/1506), and support of the Molecular Spectroscopy Facility at the Rutherford Appleton Laboratory (RAL). We thank Dr. D. Ascenzi, Dr. C. M. Western and Prof. M. N. R. Ashfold for helpful discussions, and Mr. M. Page and Mr. R. G. Williams for technical assistance at RAL.

References and Notes

(1) Rabitz, H. *Annu. Rev. Phys. Chem.* **1974**, *25*, 155.
(2) Kuze, A.; Chance, K. V. *J. Geophys. Res.* **1994**, *99*, 14481.
(3) Ball, S. M.; Hancock, G. *Geophys. Res. Lett.* **1995**, *22*, 1213.
(4) Ravishankara, A. R.; Hancock, G.; Kawasaki, M.; Matsumi, Y. *Science* **1998**, *280*, 60.
(5) Mlynczak, M. G.; Marshall, B. T. *Geophys. Res. Lett.* **1996**, *23*, 657.
(6) Wayne, R. P. *Res. Chem. Intermed.* **1994**, *20*, 395.
(7) Tarasick, D. W.; Evans, W. F. J. *Adv. Space Res.* **1993**, *13*, 145.
(8) Mlynczak, M. G.; Solomon, S.; Zaras, D. S. *J. Geophys. Res.* **1993**, *98*, 18639.
(9) Sica, R. J. *Can. J. Phys.* **1991**, *69*, 1069.
(10) Yamamoto, H.; Makino, T.; Naito, I.; Sekiguchi, H. *J. Geomag. Geoelectr.* **1989**, *41*, 1043.
(11) Noxon, J. F. *Planet. Space Sci.* **1982**, *30*, 545.
(12) Evans, W. F. J.; McDade, I. C.; Yuen, J.; Llewellyn, E. J. *Can. J. Phys.* **1988**, *66*, 941.
(13) Thomas, R. J.; Barth, C. A.; Rusch, D. W.; Sanders, R. W. *J. Geophys. Res.* **1984**, *89*, 9569.
(14) Traub, W. A.; Carleton, N. P.; Connes, P.; Noxon, J. F. *Astrophys. J.* **1979**, *229*, 846.
(15) Connes, P.; Michel, G. *Astrophys. J.* **1974**, *190*, L29.
(16) Kear, K.; Abrahamson, E. W. *J. Photochem.* **1975**, *3*, 409.
(17) Mlynczak, M. G.; Olander, D. S. *Geophys. Res. Lett.* **1995**, *22*, 1377.
(18) DeMore, W. B.; Sander, S. P.; Golden, D. M.; Hampson, R. F.; Kurylo, M. J.; Howard, C. J.; Ravishankara, A. R.; Kolb, C. E.; Molina, M. J. *Chemical Kinetics and Photochemical Data for Use in Stratospheric Modelling*, JPL publication 92-20 1992.
(19) Okabe, H. *Photochemistry of Small Molecules*; Wiley: New York, 1978.
(20) Lewis, J. S. *Physics and Chemistry of the Solar System*; Academic Press: San Diego CA 1995.
(21) Badger, R. M.; Wright, A. C.; Whitlock, R. F. *J. Chem. Phys.* **1965**, *43*, 4345.
(22) Vallance Jones, A.; Harrison, A. W. *J. Atm. Terr. Phys.* **1958**, *13*, 45.
(23) Vallance Jones, A.; Gattinger, R. L. *Plant. Space Sci.* **1963**, *11*, 961.
(24) Klotz, R.; Marian, C. M.; Peyerimhoff, S. D.; Hess, B. A.; Buenker, R. *J. Chem. Phys.* **1984**, *89*, 223.
(25) Hsu, Y. T.; Lee, Y. P.; Ogilvie, J. F. *Spectrochim. Acta A* **1992**, *48*, 1227.
(26) Mlynczak, M. G.; Nesbitt, D. J. *Geophys. Res Lett.* **1995**, *22*, 1381.
(27) Špalek, O.; Kodymová, J.; Stopka, O.; Micek, I. *J. Phys. B: At Mol. Phys.* **1999**, *32*, 1885.
(28) Miller, H. C.; McCord, J. E.; Choy, J.; Hager, G. D. *International Conference on Lasers*, Portland, Oregon, 1996.
(29) Gamache, R. R.; Goldman, A.; Rothman, L. S. *J. Quant. Spectrosc. Radiat. Transfer* **1998**, *59*, 495.
(30) Brault, J.; Brown, M. M. unpublished results cited in Ref. 29
(31) The HITRAN (High-resolution Transmission) molecular spectroscopic database and HAWKS (HITRAN Atmospheric Workstation) **1996** edition; Rothman, L. S.; Rinsland, C. P.; Goldman, A.; Massie, S. T.; Edwards, D. P.; Flaud, J.-M.; Perrin, A.; Camy-Peyret, C.; Dana, V.; Mandin, J.-Y.; Schroeder, J.; McCann, A.; Gamache, R. R.; Wattson, R. B.; Yoshino, K.; Chance, K. V.; Jucks, K. W.; Brown, L. R.; Nemtchinov, V.; Varanasi, P. *J. Quant. Spectrosc. Radiat. Transfer* **1998**, *60*, 665.
(32) Sandor, B. J.; Clancy, R. T.; Rusch, D. W.; Randall, C. E.; Eckman, R. S.; Siskind, D. S.; Muhleman, D. O. *J. Geophys. Res.* **1997**, *102*, 9013.
(33) Lafferty, W. J.; Solodov, A. M.; Lugez, C. L.; Fraser, G. T. *Appl. Opt.* **1998**, *37*, 2264.
(34) Newman, S. M.; Lane, I. C.; Orr-Ewing, A. J.; Newnham, D. M.; Ballard, J. *J. Chem. Phys.* **1999**, *110*, 10749.

(35) Cheah, S.-L.; Lee, Y.-P.; Ogilvie, J. F. *J. Quant. Spectrosc. Radiat. Transfer* **2000**, *64*, 467.
(36) Ballard, J.; Strong, K.; Remedios, J. J.; Page, M.; Johnston, W. B. *J. Quant. Spectrosc. Radiat. Transfer* **1994**, *52*, 677.
(37) Gronholz, J.; Herres, W. *Understanding FT-IR Data Processing*, Dr. Alfred Huethig Publishers 1985.
(38) Spectral simulation program PGOPHER written by Dr C. M. Western, University of Bristol. A summary of the program and the Hamiltonian used is given in Green, M. E.; Western, C. M. *J. Chem. Phys.* **1996**, *104*, 848.
(39) Chou, S.-I.; Baer, D. S.; Hanson, R. K. *J. Mol. Spectrosc*. **1999**, *195*, 123.
(40) Ritter, K. J.; Wilkerson, T. D. *J. Mol. Spectrosc*. **1987**, *121*, 1.
(41) Newman, S. M. *Ph.D. Thesis, University of Bristol* 2000.
(42) Bevington, P. R.; Robinson, D. K. *Data Reduction and Error Analysis for the Physical Sciences, 2nd edition*; McGraw-Hill: New York, 1992.
(43) Strong, E. K. *D. Phil. Thesis, University of Oxford* 1992.
(44) Bouanich, J.-P.; Blanquet, G.; Populaire, J.-C.; Walrand, J. *J. Mol. Spectrosc.* **1998**, *190*, 7.
(45) Schermaul, R.; Learner, R. C. M. *J. Quant. Spectrosc. Radiat. Transfer* **1999**, *61*, 781.
(46) Van Vleck, J. H. *Astrophys. J.* **1934**, *80*, 161.
(47) Anderson, P. W. *Phys. Rev.* **1949**, *76*, 647.
(48) Tsao, C. J.; Curnette, B. *J. Quant. Spectrosc. Radiat. Transfer* **1962**, *2*, 41.
(49) Birnbaum, G. *Adv. Chem. Phys.* **1967**, *12*, 487.
(50) Legan, R. L.; Roberts, J. A.; Rinehart, E. A.; Lin, C. *J. Chem. Phys*. **1965**, *43*, 4337.
(51) Brown, L. R.; Plymate, C. *J. Mol. Spectrosc.* **2000**, *199*, 166.
(52) Giver, L. P.; Boese, R. W.; Miller, J. H. *J. Quant. Spectrosc. Radiat. Transfer* **1974**, *14*, 793.
(53) Mélières, M. A.; Chenevier, M.; Stoeckel, F. *J. Quant. Spectrosc. Radiat. Transfer* **1985**, *33*, 337.
(54) Lewis, B. R.; Berzins, L.; Dedman, C. J.; Scholtz, T. T.; Carver, J. H. *J. Quant. Spectrosc. Radiat. Transfer* **1988**, *39*, 271.
(55) Amano, T.; Akao, K.; Oka, H.; Unno, O. *Chem. Phys. Lett*. **1999**, *311*, 433.
(56) Setzer, B. J.; Pickett, H. M. *J. Chem. Phys*. **1980**, *67*, 340.
(57) Pope, R. S.; Wolf, P. J.; Perram, G. P. *J. Quant. Spectrosc. Radiat. Transfer* **2000**, *64*, 363.
(58) Ascenzi, D. *Ph.D. Thesis, University of Perugia* 1998.
(59) Bussery, B.; Wormer, P. E. S. *J. Chem. Phys*. **1993**, *99*, 1230.
(60) Bussery-Honvault, B.; Veyret, V. *J. Chem. Phys.* **1998**, *108*, 3243.
(61) Ray, B.; Ghosh, P. N. *Spectrochim. Acta A* **1997**, *53*, 537.
(62) Ray, B.; Biswas, D.; Ghosh, P. N. *J. Mol. Struct.* **1997**, *407*, 39.
(63) Biswas, D.; Ray, B.; Ghosh, P. N. *Chem. Phys. Lett.* **1997**, *275*, 314.
(64) Seiser, N.; Robie, D. C. *Chem. Phys. Lett.* **1998**, *282*, 263.
(65) Houdeau, J. P.; Boulet, C.; Bonamy, J.; Khayar, A.; Guelachvili, G. *J. Chem. Phys.* **1983**, *79*, 1634.
(66) Gamache, R. R. *J. Mol. Specrosc*. **1985**, 1*14*, 31.
(67) Chackerian, C. *J. Mol. Spectrosc*. **1985**, *113*, 373.
(68) Gamache, R. R.; Rothman, L. S. *J. Mol. Spectrosc*. **1988**, *128*, 360.
(69) Minaev, B. F.; Lunell, S.; Kobzev, G. I. *J. Mol. Struct*. **1993**, *284*, 1.
(70) Minaev, B. F.; Ågren, H. *J. Chem. Soc., Faraday Trans*. **1997**, *93*, 2231.